Fast structural responses of gap junction membrane domains to AB5 toxins

Irina V. Majoul[a,1], Liang Gao[b], Eric Betzig[b], Daria Onichtchouk[c], Eugenia Butkevich[d], Yuri Kozlov[e], Feliksas Bukauskas[f], Michael V. L. Bennett[f], Jennifer Lippincott-Schwartz[g,1], and Rainer Duden[a,1]

[a]Institute of Biology, Center for Structural and Cell Biology in Medicine, University of Lübeck, 23562 Lübeck, Germany; [b]Janelia Farm Research Campus, Howard Hughes Medical Institute, Ashburn, VA 20147; [c]Center for Biological Signaling Studies, Albert Ludwigs University, 79104 Freiburg, Germany; [d]Drittes Physikalisches Institut, Biophysik, Georg-August-Universität, 37077 Göttingen, Germany; [e]V.A. Engelhardt Institute for Molecular Biology, Russian Academy of Sciences, Moscow 119991, Russia; [f]Dominick P. Purpura Department of Neuroscience, Albert Einstein College of Medicine, Bronx, NY 10461; and [g]Eunice Kennedy Shriver National Institute of Child Health and Human Development, National Institutes of Health, Bethesda, MD 20892

Contributed by Jennifer Lippincott-Schwartz, September 9, 2013 (sent for review June 20, 2013)

Gap junctions (GJs) represent connexin-rich membrane domains that connect interiors of adjoining cells in mammalian tissues. How fast GJs can respond to bacterial pathogens has not been known previously. Using Bessel beam plane illumination and confocal spinning disk microscopy, we found fast (~500 ms) formation of connexin-depleted regions (CDRs) inside GJ plaques between cells exposed to AB5 toxins. CDR formation appears as a fast redistribution of connexin channels within GJ plaques with minor changes in outline or geometry. CDR formation does not depend on membrane trafficking or submembrane cytoskeleton and has no effect on GJ conductance. However, CDR responses depend on membrane lipids, can be modified by cholesterol-clustering agents and extracellular K^+ ion concentration, and influence cAMP signaling. The CDR response of GJ plaques to bacterial toxins is a phenomenon observed for all tested connexin isoforms. Through signaling, the CDR response may enable cells to sense exposure to AB5 toxins. CDR formation may reflect lipid-phase separation events in the biological membrane of the GJ plaque, leading to increased connexin packing and lipid reorganization. Our data demonstrate very fast dynamics (in the millisecond-to-second range) within GJ plaques, which previously were considered to be relatively stable, long-lived structures.

membrane traffic | connexin actin | cell–cell junctions | cholesterol

Highly permeable biological membrane domains composed of assemblies of connexin channels form gap junction (GJ) plaques at cell–cell interfaces (1–3). The cell–cell connectivity provided by GJs helps individual cells integrate functionally into tissues via electrical coupling (4, 5) and diffusion of signaling molecules and metabolites (6, 7). GJs critically determine permeability to Ca^{2+}, cAMP, cGMP, IP3, glutathione, and other metabolites smaller than 1.5 kDa (6, 8, 9). Formation of GJs requires vesicular transport and in some cases Golgi-dependent posttranslational modifications of connexins (10). GJ turnover involves endocytosis and proteasomal/lysosomal degradation (11–14). During infection and under stress conditions the level of signaling molecules is elevated dramatically, and how signaling via GJs is modulated between affected cells remains unclear.

High-speed live-cell microscopy revealed early responses of GJ plaques to purified AB5 toxins normally released by the human pathogens *Vibrio cholerae*, *Shigella dysenteriae*, and enterohemorrhagic *Escherichia coli* (EHEC). In this study we used both Bessel beam plane illumination microscopy (15) and spinning disk confocal microscopy. Because GJ responses are rapid, and because GJ plaques often are curved, the high-speed and near-isotropic 3D resolution (~300 nm) of Bessel beam plane illumination microscopy was beneficial in revealing the responses in 4D spatiotemporal detail. (The experimental setup is shown in Fig. 1 *A* and *B*; also see *SI Appendix*, Fig. S1. For further details, see ref. 15.)

To study GJ responses, we applied purified fluorescently labeled AB5 toxins, namely cholera toxin (CTX), Shiga toxin type 1 (STx1), or Shiga toxin type 2 (STx2, also known as Vero-toxin and released by EHEC bacteria), according to protocols we have described previously (16–18). CTX and STx1 both consist of a homopentameric B-subunit and a catalytic A-subunit (for a schematic structure see Fig. 1*C*). The five identical B-subunits are responsible for binding to the plasma membrane via specific glycosphingolipids [CTX binds to monosialotetrahexosylganglioside (GM1), and STx1 to globotriaosylceramide (Gb3)]. For each molecule of CTX or STx1, several glycosphingolipid molecules can be bound at the same time (up to 15 molecules of Gb3 for STx1), and thus these toxins have the potential to induce lipid reorganization (19). As a model system, we used Vero cells (African green monkey kidney fibroblasts) and HeLa cells (a human cervical carcinoma cell line) transfected with different fluorescently tagged connexin isoforms, as described earlier (20, 21).

Optical sectioning using Bessel beam plane illumination microscopy operating in structured illumination mode (Bessel OS-SIM) (15) at an acquisition speed of approximately one 3D volume stack/20 s revealed dramatic responses of GJ plaques to AB5 toxins. Strikingly, application of CTX to Vero cells coupled by fluorescently labeled connexin isoform 30 (Cx30-EGFP) GJs rapidly induced regions within the GJ plaque that were depleted of Cx30-EGFP fluorescence (hereafter referred to as transient connexin-depleted regions, tCDRs) (Fig. 1 *D–I*, *SI Appendix*, Fig.

Significance

We used 3D Bessel beam plane illumination and spinning disk microscopy to reveal fast structural changes in the architecture of gap junctions (GJs). Previously, GJ plaques were considered relatively stable structures. We demonstrate extremely rapid remodeling of proteins and lipids within GJ plaques in response to bacterial toxin exposure. Connexin channels within GJ plaques undergo dramatic rearrangements that lead to increased connexin packing and lipid reorganization. These changes likely reflect lipid-phase separation events in the biological membrane. Toxin-induced connexin reorganization depends on lipids and is little modified by membrane–cytoskeletal interactions. We suggest that fast GJ changes upon toxin exposure reveal an early-response system of cells and that GJ plaques are much more dynamic structures than previously recognized.

Author contributions: I.V.M., F.B., and R.D. designed research; I.V.M., L.G., F.B., and R.D. performed research; I.V.M., L.G., E. Betzig, D.O., E. Butkevich, Y.K., F.B., and J.L.-S. contributed new reagents/analytic tools; I.V.M., L.G., E. Betzig, D.O., E. Butkevich, Y.K., F.B., M.V.L.B., J.L.-S., and R.D. analyzed data; and I.V.M., D.O., F.B., M.V.L.B., J.L.-S., and R.D. wrote the paper.

The authors declare no conflict of interest.

Freely available online through the PNAS open access option.

[1]To whom correspondence may be addressed. E-mail: irina.majoul@bio.uni-luebeck.de, lippincj@mail.nih.gov, or duden@bio.uni-luebeck.de.

This article contains supporting information online at www.pnas.org/lookup/suppl/doi:10.1073/pnas.1315850110/-/DCSupplemental.

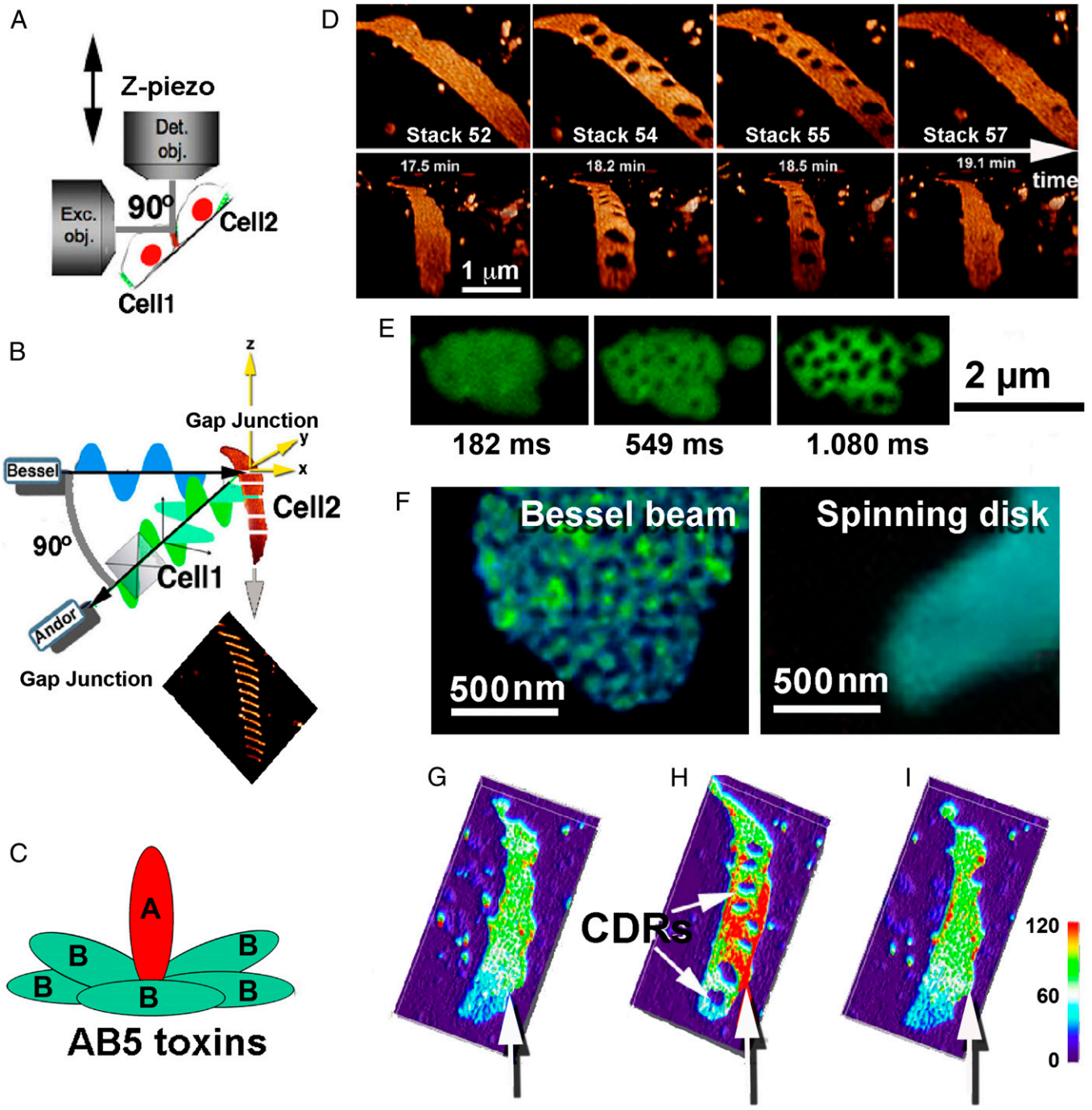

Fig. 1. Super Resolution Bessel beam plane illumination microscopy reveals dynamic structural rearrangements within GJ plaques in response to AB5 toxins. (*A* and *B*) Schematics showing the experimental setup. The Bessel beam produced by an excitation objective (Exc. obj.) is swept rapidly over successive planes along the *z*-axis, and the focal plane of a detection objective (Det. obj.) follows. Fluorescence detection is done using an EM-CCD (Andor) camera (for details, see ref. 15). Two contacting cells with GJ plaques formed between them are indicated as Cell1 and Cell2. The tilted orientation of the coverslip in this microscope setup allowed us to use gravitational force to apply and remove bacterial toxins rapidly. (*C*) Schematic structure of AB5 toxins with the catalytically active A-subunit inserted into the homopentameric B-ring. (*D*) Application of CTX induces the formation and recovery of tCDRs inside a Cx30-EGFP–labeled GJ plaque. Selected frames from the 4D Bessel beam microscopy data stack are shown. (The full dataset is shown in Movie S1). Note that the same GJ plaque recorded as 3D data stacks over time is shown from different viewing perspectives in the upper and lower panels. (*E*) Fast kinetics of tCDR formation was measured by spinning disk microscopy with a free run of an Andor EM-CCD camera. Note that tCDRs develop inside the Cx30-EGFP plaque within a few hundred milliseconds, with a maximal toxin response obtained less than 1 s after the initiation of the process. (*F*) Cx30-FP–labeled GJ plaques in two comparable cell samples imaged with Bessel beam plane illumination microscopy (*Left*; Cx30-GFP) or confocal spinning disk microscopy (*Right*, CX30-CFP). Note that puncta-like substructures inside the GJ plaque can be visualized only with Super Revolution Bessel beam plane illumination microscopy, whereas spinning disk microscopy shows only unresolved smooth fluorescence. (*G–I*) tCDR formation increases local fluorescence intensities in surrounding regions within the GJ plaque. (*G*) Before toxin. (*H*) Full toxin action at 2 s. (*I*) After tCDR recovery at ∼1 min. Vertical white arrows point to regions with visible changes in intensity, consistent with a closer packing of connexin channels in regions outside tCDRs. However, neither tCDR formation or recovery significantly changes the total integrated fluorescence measured over the entire 3D structure of the GJ plaque (*SI Appendix*, Fig. S1*C*).

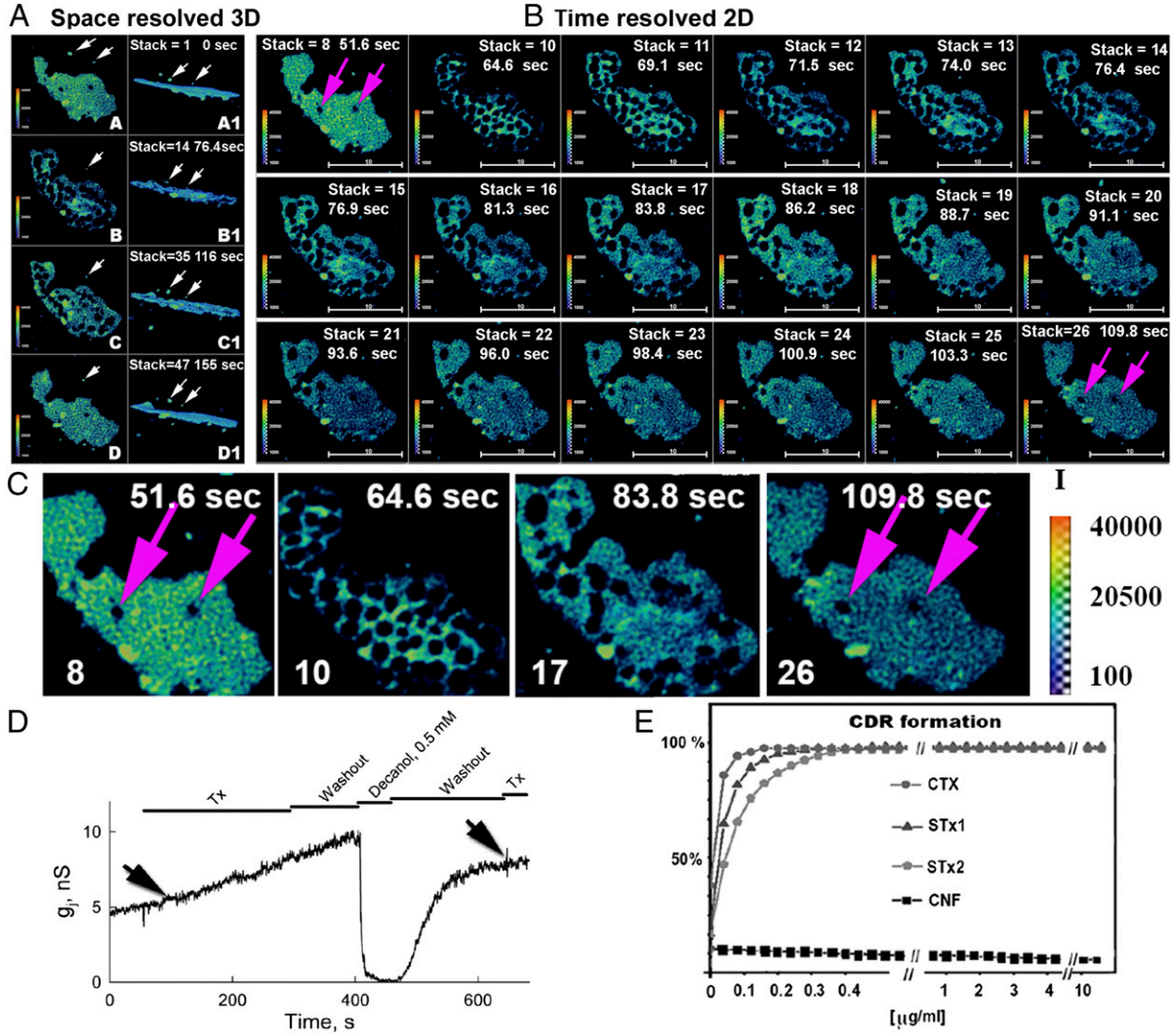

Fig. 2. Bessel beam microscopy resolution of tCDRs induced by STx1 and their recovery. Formation of tCDRs does not change the 3D organization of the GJ plaque, and sCDRs reappear at the same positions. (*A*) Rapid tCDR formation dramatically changes the appearance of the GJ plaque (compare subpanels *A* and *A1* with subpanels *B* and *B1*) but does not change the 3D geometry or the outer shape of the GJ plaque. Subpanels *A1–D1* and subpanels *A–D* are representative frames from the same 4D stack from different viewing angles [i.e., *en face* view (in subpanels *A–D*) and side view (in subpanels *A1–D1*) (Movies S2 and S3)]. A first pulse of STx1 toxin was added at ∼70 s (subpanels *A* and *A1*). Note the dramatic tCDR formation that is complete at frame 2 (subpanels *B* and *B1*). A second pulse of Stx1 was applied at 116 s (after CDRs had recovered completely from the first pulse of AB5 toxin pulse) and again induced tCDR formation (subpanels *C* and *C1*). Note that tCDR formation induced by the second pulse of AB5 toxin occurs in local regions of the GJ plaque that are different from the ones induced by the previous pulse of AB5 toxin. Images in subpanels *D* and *D1* show the GJ plaque after recovery from the second wave of tCDR formation (i.e., ∼40 s after application of the second wave of STx1). The sequence in subpanels *A1–D1* also reveals that some membrane structures containing Cx43-GFP (indicated by white arrows) remain at the same positions in 3D space during formation and recovery of tCDRs within the time of image acquisition (442 s). The exocytic/endocytic nature of these vesicles was not determined in this experiment. (*B*) Surface view ("Time resolved 2D") of time-dependent changes within the GJ plaque during tCDR formation and recovery. Two sCDRs are indicated by pink arrows in the first and last frame. This 4D dataset was acquired using the two-photon mode of Bessel beam plane illumination microscopy, depicting the response and recovery of a GJ plaque to one pulse of CTX application. 3D image stacks (a total of 134) were acquired every 5 s, covering a total time period of 442 s. The color key in the images indicates the distribution of fluorescence intensities within the GJ plaque at different time points after CTX application (yellow/red indicates high fluorescence intensity; blue/green indicates lower intensity). Times in seconds and stack numbers are indicated. (*C*) Higher-magnification views of frames 8, 10, 17, and 26 from *B* (corresponding to Movie S2). Pink arrows indicate sCDRs. Note that these sCDRs disappear when tCDRs are formed and reoccur at the same positions within the GJ plaque after tCDR recovery. (*D*) No changes in g_j were detected upon CTX application (marked by arrows) in a pair of HeLa cell expressing Cx36-EGFP with a dual whole-cell voltage clamp. Decanol-induced decrease of g_j between Cx36 GJs with partial reversal demonstrates that the coupling did not result from cytoplasmic bridges. A second application of CTX also had little effect on g_j. (*E*) Comparative potency of different toxins toward tCDR induction. (For further details on toxins used, see *SI Appendix*, Table S1.) In contrast to AB5 toxins, the non-AB5 toxin CNF produced by pathogenic *E. coli* did not cause tCDR formation.

S2, and Movies S1–S3). tCDRs were approximately circular and reached maximum size within a few hundred milliseconds after the beginning of the process, as recorded with fast spinning disk microscopy (Fig. 1*E*, *SI Appendix*, Fig. S2, and Movie S5). In contrast to the smooth fluorescence of GJ plaques observed with spinning disk microscopy (Fig. 1*F*, *Right*; also see Fig. 3), the superior resolution of Bessel beam microscopy in structured illumination mode clearly demonstrated dynamic substructures (i.e., puncta) that may represent clusters of connexin channels that move within the plane of the GJ plaque (Fig. 1*F*, *Left*, Fig. 2, and Movie S2). Local fluctuations in fluorescence intensity appeared in accord with newly formed tCDRs. Fluorescence

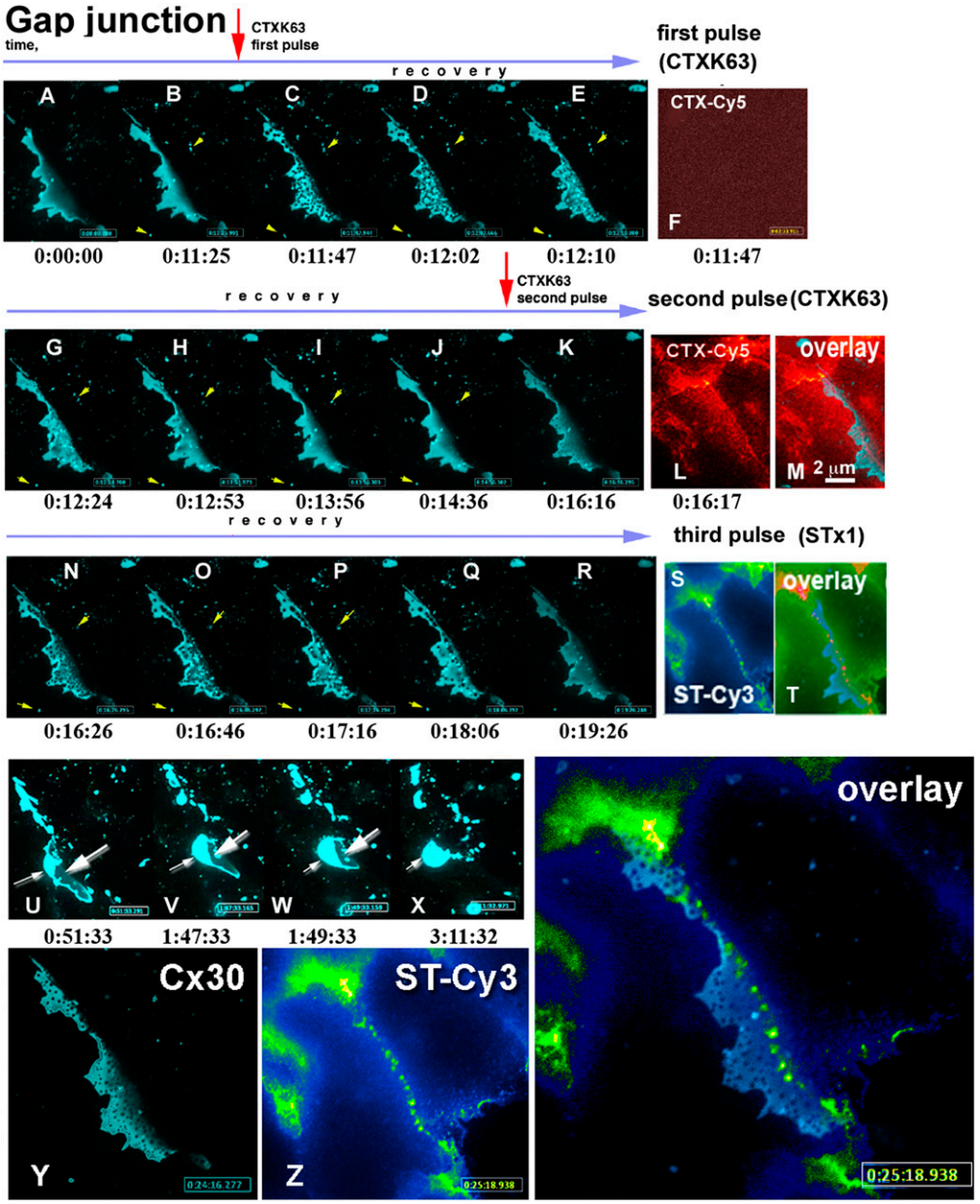

Fig. 3. tCDRs are not formed due to the direct binding of AB5 toxins to GJ plaques, but appear as part of a generalized response of the cell membranes to stress induced by the toxins. (*A*–*R*) (blue) Fluorescence of a Cx30-CFP labeled GJ plaque over time in the same confocal *z* plane (the entire process can be followed in Movie S4). Red arrows indicate the times of addition of a Cy5-labeled nontoxic mutant of CTX, CTXK63. Fast appearance of tCDRs (*B* and *C* frames) was followed by comparatively slow recovery, lasting around 1 min (*E*–*H*). Cx30-CFP labeled membrane vesicles (yellow arrowheads) next to the GJ plaque remained intact, their positions stayed unchanged during tCDR formation and recovery. (Only one vesicle disappeared between *H* and *I*, presumably from the focal plane.) (*F*) No plasma membrane labeling with Cy5-labeled CTX was detected during the first period of tCDR formation, suggesting that few molecules of toxins are sufficient to generate a tCDR response. (*L*) Membrane surface fluorescence was only observed after a second application of Cy5-labeled toxin. (*M*) Spectrally distinct channels were selected for Cx30-CFP (λex = 434 nm) and CTX-Cy5 (λex = 647 nm) to exclude bleed-through of the fluorescence. This data confirms absence of colocalization between toxin and GJ plaque or between toxin and tCDRs that appeared inside the GJ plaque. Time is indicated below individual movie frames as hours:minutes: seconds. (*K*–*R*) The second application of (CTXK63-Cy5) to the same plaque again resulted in fast tCDR formation and slow recovery (see also *SI Appendix*, Fig. S6). After recovery from two pulses of CTX, wild-type STx1 toxin labeled with Cy3 (ST-Cy3) induced a third round of tCDR formation and recovery in the same GJ plaque (not shown here; see Movie S4). (*S* and *T*) As with CTXK63-Cy5, the fluorescence of Cy3-STx1 was not colocalized with tCDRs inside the Cx30-CFP–labeled GJ plaque or in the plaque itself. (*T*) Three-channel overlay of R and S: note that the color table was adjusted to better display that neither toxin colocalized with the Cx30-CFP fluorescence of the GJ plaque. Cx30-CFP is shown in blue; red structures represent colocalization of both toxins. (*U*–*X*) Three pulses of AB5 toxins resulting in three waves of tCDR responses induced irreversible changes in the contacting cells. Further observation of the same GJ plaque over the next 5.5 h revealed disruption of the cell–cell contact and internalization of the GJ plaque (Movie S4). [Scale bar in M (2 μm) defines sizes for all images in *A*–*X*.] (*Y* and *Z*) Higher-magnification view of the tCDR response induced in the Cx30-CFP–labeled GJ plaque. An overlay of Cx30-CFP (*Y*) and STx1 (*Z*) fluorescence is shown, demonstrating that STx1 and tCDRs do not colocalize; times are indicated. (For the complete data set and further details see Movie S4.)

intensity was increased locally in the regions surrounding tCDRs (compare Fig. 1 *G* and *H*; see white vertical arrows). Washout of the toxin induced recovery of tCDRs within seconds to minutes, and the distribution of fluorescence intensity became homoge-

nous again (compare Fig. 1 *H* and *I*). During these processes the size and outline of the GJ plaque remained very much the same, and the overall fluorescence, as recorded with 3D image stacks, did not change significantly (*SI Appendix*, Fig. S1*C*).

We tested whether tCDR formation and/or recovery induces changes in the 3D organization of the GJ plaque and whether either event is accompanied by the delivery of new membrane material from the interior of the contacting cells. To do so, we monitored Cx36-EGFP–labeled GJ plaques upon application of STx1 in 4D using the two-photon mode of Bessel beam plane illumination microscopy (Fig. 2 *A* and *B* and Movies S2 and S3). We observed that the 3D organization of the GJ plaque changed very little during the dramatic tCDR formation and recovery, even after two pulses of AB5 toxin treatment (Fig. 2*A*: compare *en face* views in subpanels *A–D* with side views in subpanels *A1–D1*). During the formation or recovery of tCDRs, membrane vesicles labeled with Cx36-EFGP (some are indicated by white arrows) did not change positions relative to the GJ plaque, indicating that they did not contribute to either event. However, whether vesicle-trafficking events/machineries have a role in the fast dynamics of GJ plaques induced by AB5 toxin will require further study in future experiments.

Given that local fluorescence increases in the regions surrounding tCDRs during tCDR formation and decreases upon tCDR recovery (Fig. 1 *G–I*), we hypothesize that tCDRs are formed by the migration of channels out of the forming tCDRs into neighboring regions within the GJ plaque, resulting in denser clustering of connexins in these regions. Remarkably, the size and shape of the GJ plaque did not change during tCDR formation and recovery (Fig. 2 *A* and *B*). When GJ plaques harbored preexisting stationary CDRs (sCDRs), they reappeared at the same positions in the plaque upon recovery of toxin-induced tCDRs (Fig. 2 *B* and *C*, pink arrows on the first and the last image of the sequence, respectively). sCDRs have been observed previously by Falk et al. (22) and referred to as "circular nonfluorescent domains," which can persist for hours and finally may be expelled at GJ plaque edges. In this study, we observed that formation of long-lived sCDRs can be induced in response to lipid-acting chemical agents such as octanol and dimethylformamide (*SI Appendix*, Fig. S3). Thus, at least two different types of CDRs are found in GJ plaques: toxin-induced tCDRs and sCDRs, showing that GJ plaques are much more pliable membrane domains than previously assumed, even on very fast time scales as we present here.

Application of two different members of the AB5 toxin family, namely CTX (Figs. 1 and 2), and STx1 (Fig. 3), each induced very fast tCDR formation in GJ plaques in cells expressing connexins labeled with fluorescent proteins. However, application of a non-AB5 family toxin produced by *Escherichia coli*, namely cytotoxic necrotizing factor 1 (CNF), did not induce a CDR response (Fig. 2*E*, and *SI Appendix*, Table S1). Thus, toxin-induced tCDRs represent a unique way in which GJ plaques respond to AB5 toxins. The generalized response of the entire GJ plaque to AB5 toxins is likely to involve the rearrangement of membrane lipids and phase separation events within the membrane (for discussion, see ref. 23). Further, tCDR formation appears to be accompanied by a change in the packing density of connexin channels within the GJ plaque.

We wished to determine whether tCDR responses induced by AB5 toxins in GJ plaques affect junctional conductance (g_j). We combined dual patch-clamp recording to measure g_j in cells expressing Cx36-EGFP (24) with fluorescence imaging during toxin application (Fig. 2*D* and *SI Appendix*, Fig. S5). Contrary to our expectation, g_j did not change during formation of tCDRs and their recovery (Fig. 2*D* and *SI Appendix*, Fig. S5). Largely reversible GJ uncoupling induced by decanol (0.5 mM) confirmed that, for the same pair of cells, the measured g_j indeed derived from GJs and not from cytoplasmic bridges. An absence of changes in GJ electrical conductance upon application of AB5 toxins also was observed in cells expressing the fluorescently labeled connexin isoforms Cx43-EGFP or Cx47-EGFP (*SI Appendix*, Fig. S5). Electrophysiological data were replicated with different connexin isoforms (*SI Appendix*, Table S1) and confirmed the stability of intercellular coupling during the initial phases of AB5 toxin application and tCDR formation.

We further tested whether application of AB5 toxins induced changes in intracellular calcium, using fluorescent imaging with the indicator dye Fluo-4. We did not observe any immediate responses (i.e., on the fast time scale equal to tCDR formation); instead, we recorded relatively slow increases in intracellular calcium over time (within 20–30 s) upon repeated AB5 toxin treatments (*SI Appendix*, Fig. S7).

To analyze with higher time resolution the kinetics of fast responses of GJ plaques to repeated application of AB5 toxins, we used fast switching of three laser lines combined in a spinning disk confocal microscopy setup (Fig. 3 and Movie S4). To explore whether AB5 toxins are localized physically within newly formed tCDRs. we sequentially applied toxins labeled with different dyes, with colors complementary to CFP-tagged connexins. STx1-Cy3 or CTX-Cy5 (with both the A- and B-subunits labeled) were applied to cells coupled by Cx30-CFP GJ plaques (Fig. 3). The first application of a nontoxic point mutant variant of CTX, CTXK63 (described by us in refs. 16 and 17), resulted in rapid and dramatic formation of tCDRs (Fig. 3 *A–E*). We used a laser switch to correlate CDR formation with the speed of immobilization of labeled toxin on the plasma membrane. To our surprise the first tCDRs appeared much faster than we were able to detect any fluorescence of immobilized toxin anywhere on the cell membrane (compare Fig. 3 *C* and *F*). After tCDR recovery (Fig. 3 *G–J*) a second pulse of CTXK63 again caused tCDR formation (Fig. 3*K*). At this time point we could see toxin immobilized on the plasma membrane (Fig. 3*L*). However, toxin fluorescence did not colocalize with the tCDRs formed in the GJ plaque at any time (Fig. 3 *K* and *M*, overlay and *SI Appendix*, Fig. S6). For the third pulse of toxin we used another member of the AB5 family, STx1 (Fig. 3 *N–S* and overlay in *T*). Again, no colocalization between tCDRs and toxin was detected. These results are clearly visible at high magnification (Fig. 3 *Y* and *Z* and the accompanying two-channel overlay).

To test possible cellular factors involved in the tCDR response, we destroyed the submembrane cytoskeleton by depolymerizing actin with the drug latrunculin A. Disassembly of the actin-containing submembrane cytoskeleton did not prevent the AB5 toxin-induced formation of tCDRs (data for STx1 are shown in *SI Appendix*, Fig. S4), which occurred with kinetics very similar to those in untreated cells. However, unlike GJ plaques in untreated cells, the geometry of the GJ plaques in cells treated with latrunculin A changed dramatically upon the application of AB5 toxin (*SI Appendix*, Fig. S4 *D–J*). Additionally, the remarkable reappearance of sCDRs at the same positions in GJ plaques after tCDR recovery reported here (Figs. 2 and 3) also demonstrates that GJ plaque geometry in cells is stable against perturbations occurring within the plaque membrane. Actin is a prominent component in near proximity to GJ plaques, as has been shown by EM studies in eye lens cells (25). We previously demonstrated a stabilizing role of the actin-binding protein drebrin for GJ plaques (20). We suggest here that GJ plaque size and shape are stabilized and changed in an actin/drebrin-dependent manner by the underlying submembrane cytoskeleton.

To test further whether tCDR formation somehow may affect GJ-mediated cell–cell signaling, we transfected cells with the FRET-based cAMP Epac sensor system first introduced by Ponsioen et al. (26). For a fast CFP-YFP–based FRET readout in living cells forming GJ contacts, we used an Optosplit system (*SI Appendix*, Figs. S8–S12). We observed that, in contrast to noncoupled cells, two cells coupled by GJ contacts displayed synchronous changes in cAMP fluctuations over time (*SI Ap-*

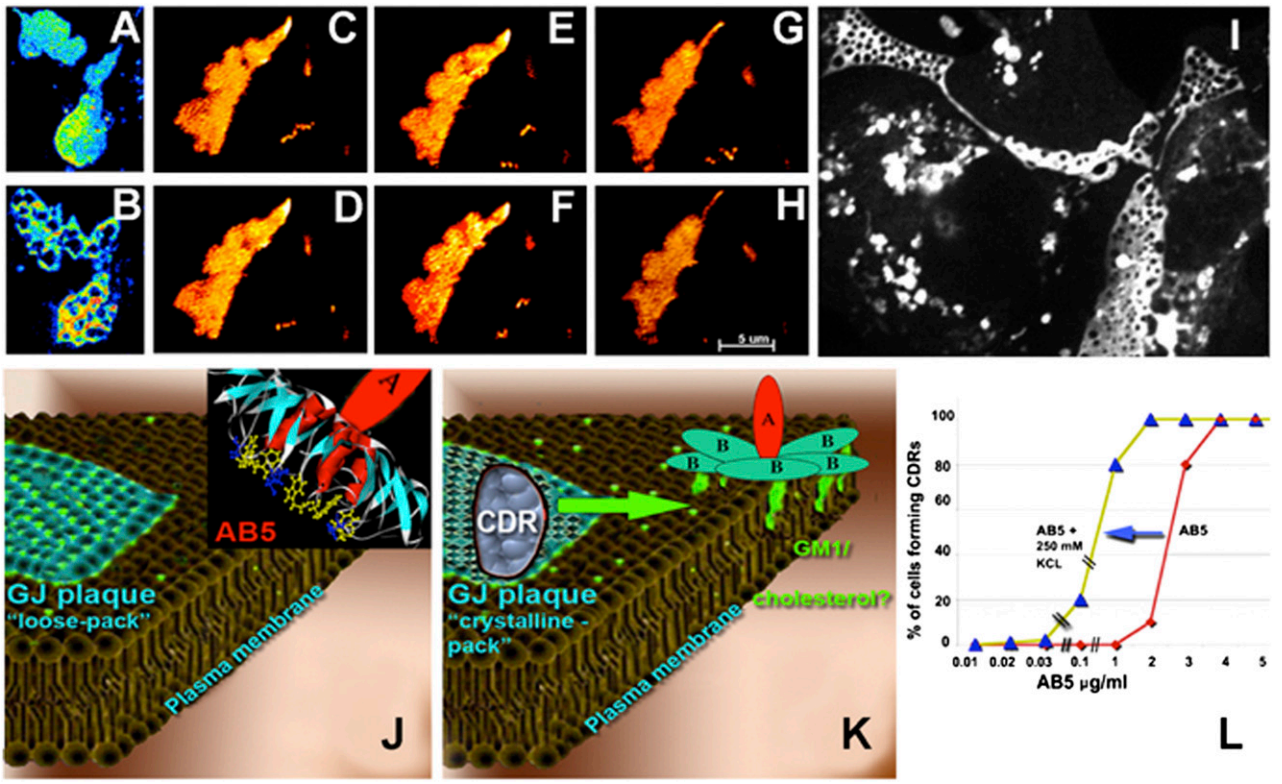

Fig. 4. Filipin prevents AB5 toxin-induced tCDR formation. Elevated external K^+ facilitates tCDR formation. (*A* and *B*) CTX induced tCDR formation in GJ plaques in control Vero cells expressing Cx43-EGFP. (*A*) Before toxin. (*B*) Twenty seconds after toxin addition. (*C*–*H*) Cx43-EGFP GJ plaques in cells pretreated with 10 µg/mL filipin for 30 min did not form tCDRs upon application of either CTX or STx1. Two pulses of CTX (*C* and *D* and *E* and *F*, respectively) followed by a pulse of STx1 (*G* and *H*) did not result in any tCDR formation. *C*, *E*, and *G* are images before toxin application; *D*, *F*, and *H* show time points 20 s after toxin addition. (*I*) Generalized tCDR responses induced by STx1 propagated along large surfaces of several GJ plaques in Vero cells expressing Cx43-EGFP. (*J* and *K*) Hypothetical view of the processes underlying tCDR formation. Toxin-induced CDR formation (*J*-to-*K* transition) is likely to be initiated inside the GJ plaque when lipids/lipid receptors move out of the plaque as AB5 toxins initiate glycosphingolipid clustering. It is conceivable that, in compensation, other lipids move into the GJ plaques, increasing the plasticity of GJ cell–cell contacts and preventing their rupture. (*L*) Diagram describing the sensitization of GJ plaques to tCDR formation in the presence of different CTX and extracellular K^+ concentrations. At increased extracellular K^+ concentrations, significantly lower toxin concentrations are required to induce tCDRs. Note that K^+ levels can be elevated naturally by toxin-induced necrotic death of neighboring cells.

pendix, Fig. S12). We found that with two or three applications of AB5 toxin, each resulting in tCDR formation (Fig. 3 *A*–*R*, Movie S1 acquired with Bessel beam microscopy, and Movie S4 acquired with spinning disk confocal microcopy), cells that initially were coupled by GJs lost synchrony in cAMP oscillations. Temporally resolved live-cell imaging of cells that initially were coupled by GJs revealed that repeated exposure to AB5 toxins resulted in the loss of synchronicity in cAMP oscillations (*SI Appendix*, Fig. S12). This loss of synchronicity (which may be preceeded by decrease in junctional conductance) often was followed by physical removal (i.e., internalization) of parts of or the entire GJ plaque from the cell–cell interface (Fig. 3 *U*–*X* and the corresponding frames in Movie S4). Internalization occurred through the invagination of the plasma membrane, presumably by clathrin-mediated endocytosis as described by the Falk group (27). After several rounds of tCDR formation induced by AB5 toxins, the irreversible changes resulted in cell death. Cell death induced by the disruption of lipid raft and microdomain signaling at the plasma membrane recently has been recognized and documented by other groups (23, 28, 29).

Slow changes in connexin density inside the GJ plaques have been documented in freeze-fracture EM studies during chick lens cell differentiation (30). Developmental changes in GJ plaques are attributed to changes in the relative abundance of cholesterol, the main component of lipid rafts, and similar changes were induced in GJs upon experimental depletion of cholesterol (30). Because of the absence of colocalization between AB5 toxins at the plasma membrane and the newly formed tCDRs inside the GJ plaque (Fig. 3 and *SI Appendix*, Fig. S6), we hypothesize that the fast tCDR response of GJ plaques to AB5 toxins results from the redistribution of cholesterol and lipid receptor complexes (GM1 and Gb3, respectively) from the region of the GJ plaque to noncontacting parts of the plasma membrane. To explore this possibility, we tested the effects of the cholesterol-sequestering drug filipin (31–35) on the efficacy of tCDR formation. Filipin treatment has been shown to disrupt clathrin-independent endocytosis in many cell types (32, 33). A pretreatment of cells with filipin (10 µg/mL for 30 min at 37 °C) did not visibly affect the size or outline of GJ plaques. However, filipin strongly reduced the formation of tCDRs induced by CTX (Fig. 4 *C*–*F*) or STx1 (Fig. 4 *G* and *H*), whereas control cells not treated with filipin readily formed tCDRs (Fig. 4 *A* and *B*). These data argue that tCDR formation is dependent on cholesterol. Perhaps cholesterol molecules clustered by filipin are unable to move within or out of the GJ plaques, thus impairing tCDR formation. (A hypothetic view is shown in Fig. 4 *J* and *K*.)

Filipin also significantly reduces K^+ influx (34, 35), so we examined whether an increase of the electrochemical gradient for K^+ across the membrane blocks the filipin-induced block of CDR formation. To test this possibility, we reduced the concentration of CTX or STx1 below the level required for CDR formation in control conditions and then gradually increased extracellular K^+ in the medium from 10 mM to 250 mM (being aware that the gradient across the plasma membrane first will

decrease, then will change in sign, and then will increase again). Remarkably, the externally added K^+ facilitated tCDR formation even when the concentration of CTX was reduced almost by 10-fold (Fig. 4*L*). Formation of tCDRs in the presence of a low AB5 toxin concentration/high K^+ gradient (Fig. 4*L*) supports the idea that tCDR formation results from the rapid movement out of the GJ plaque of cholesterol/glycosphingolipid complexes that are still mounted in the plasma membrane and are not yet internalized. However, experimental tools to test this idea currently are lacking. Deeper understanding of toxin-induced tCDR effects at the cellular level will allow prediction of how AB5 toxins may facilitate cellular loss of K^+ during bacterial infection. It remains unclear how GJ plaques release or absorb cholesterol or complexes of cholesterol/glycosphingolipids (such as GM1 or Gb3) during tCDR formation and recovery and how cholesterol movement may affect intracellular GJ signaling between infected cells. Interestingly, preventing tCDR formation by treating cells with the cholesterol-sequestering drug filipin decreased the cellular processing of inactive A-subunits of AB5 toxins into their reduced and enzymatically active forms (*SI Appendix*, Fig. S13). In future experiments we aim to look at tCDRs with EM-based methods, such as cryoelectron tomography (36) and freeze-fracture EM (30), to assess the changes to GJ plaques upon AB5 toxin action with higher spatial resolution.

In summary, using Bessel beam plane illumination microscopy, we demonstrate dynamic substructures within GJ plaques that are not observable with conventional diffraction-limited fluorescence microscopy. Using multiple laser lines in spinning disk confocal microscopy, we measured the kinetics of tCDR formation and cAMP fluctuations in GJ-coupled cells upon the application of different fluorescently labeled AB5 toxins. The data suggest that fast formation of tCDRs (i.e., connexin-depleted regions within GJ plaques) proceeds via the rearrangement and denser clustering of connexin channels within the GJ plaque in response to AB5 toxins. The identification of tCDR effects induced by AB5 toxins allows us to predict how cellular loss of K^+ may facilitate a cascade of signaling events during bacterial infection. Although speculative, it is tempting to suggest that tCDR formation, perhaps through a lipid-mediated signaling mechanism, may provide cells with an early sensing of their exposure to bacterial AB5 toxins. Finally, our data provide strong evidence that GJ plaques are much more dynamic cellular membrane domains than considered previously.

Materials and Methods

Materials. 8-Bromoadenosine 3′,5′-cyclic monophosphate, forskolin, and prostaglandin E1 were purchased from Sigma Chemical Co., 3-isobutyl-1-methylxanthine (IBMX) was purchased from Merck, and adenosine-3′,-5′-cyclic-monophosphate (NPE-caged cAMP) was purchased from Molecular Probes/Invitrogen. Unless indicated otherwise, AB5 toxins, connexins tagged with fluorescent proteins (FP), and other constructs, antibodies, and chemicals used in this study were characterized previously and described in refs. 16, 17, 20, 21, and 37. The following AB5 toxins were used (*SI Appendix*, Table S1): CTX; a nontoxic CTX mutant, CTX-K63 (16); STx1 (38); Stx2 (39); and a heat-labile enterotoxin, WT LT-1 (40). AB5 Shiga toxins were produced and purified in the Y.K. laboratory as described earlier (38). CTX AB5 forms and mutants have been characterized earlier (16, 17, 37). In addition, we used only the B-subunits of CTX and Stx1 (i.e., CTX-B and STx1-B). As a non-AB5 toxin, CNF was used (a generous gift from K. Aktories, University of Freiburg, Freiburg, Germany).

Cell Culture, Transfections, Microscope Setup for Live-Cell Imaging, and Ab5 Toxin Treatments. Vero cells (an African green monkey kidney fibroblast line) were grown and maintained in DMEM supplemented with 10% FCS (Sigma), 100 U/mL streptomycin, 100 U/mL penicillin, and 1% nonessential amino acids at 37 °C under 9% CO_2. Transient transfection of cells with expression constructs encoding fluorescent chimeric proteins, DNA cloning, and plasmid purification were done essentially as described (37). Transiently transfected Vero cells were plated on glass coverslips and imaged using a laser confocal spinning disk microscope system based on a Nikon Ti Eclipse microscope (www.nikoninstruments.com/en_DE/Products/Microscope-Systems/Inverted-Microscopes/Eclipse-Ti) equipped with a Yokogawa CSU-X1 unit (www.yokogawa.com/scanner/products/csuX1e.htm) and an Andor iXon+ EM-CCD camera. The microscope was fitted with 40×, 1.30 NA and 100×, 1.49 NA objectives. Image acquisition was controlled with Andor Bioimaging software (Andor IQ2.1). Basic control experiments and Ca^{2+} measurements were done using an Optosplit system (AcalBfi, www.acalbfi.com/uk) combined with the CSU-X1, the fastest currently available spinning disk unit with a scanning speed close to 2- to 3-ms full-frame spinning. The Bessel beam plane illumination microscope setup has been described in detail in ref. 15. Procedures for fluorescent labeling of AB5 toxins and treatment of cells with such AB5 toxins were described earlier (16, 17). For application of STx1, STx2, and CTX toxins, 10 μL of a stock solution of 3 μg/mL of labeled toxin (i.e., about 30 ng of toxin) was applied to 70% confluent cell monolayers so that after final dilution in the culture medium (~2 mL) a concentration of ~15 ng/mL was achieved. After the tCDR effect was triggered, applied toxin was washed away with freshly added medium.

Purification and Labeling of AB5 Toxins: Purification of Shiga Toxins STx1 and STx2. Crude toxin extracts were transferred on blue Sepharose for chromatography. Crude extract was prepared from exponentially growing cells of *E. coli* strains containing WT expression plasmids spSHT1 and pST23 or B-subunits or the mutated form of A-subunit expression plasmids. Cells were grown in lysogeny broth supplemented with 50 μg ampicillin/mL, harvested by centrifugation, washed with 20 mL buffer [10 mM Tris·HCl (pH 8), 10 mM NaCl, 1 mM EDTA] and resuspended in 20 mM Tris·HCl (pH 10.5), 1 mM EDTA, followed by incubation at 50 °C for 10 min. Cellular debris was removed by centrifugation at 14,000 × *g* for 30 min. The pH of the clarified supernatant was adjusted, and 0.01 volumes of 1 mg/mL PMSF in DMSO were added. This crude extract contained about 90% of the total cytotoxic material.

The crude extract was diluted twofold with 10 mM Tris·HCl (pH 7.4), 1 mM EDTA and applied to a column of AffiGel Blue (Pharmacia) equilibrated in the same buffer. After the column was washed, toxin was eluted with a 100–800 mM NaCl gradient in the same buffer. The pooled fractions containing cytotoxic material were concentrated in an Amicon ultrafiltration cell with PM30 membrane and dialyzed against 25 mM Tris acetate (pH 8.3). Dialyzed material was applied to a column of poly buffer exchanger, PBE 94 (Pharmacia Fine Chemicals), that had been equilibrated with 25 mM Tris acetate (pH 8.3). After the column was washed with two column volumes of the same buffer, material was eluted with poly buffer 96 (pH 6.0). Fractions containing toxin were collected, and the protein was precipitated by adding solid ammonium sulfate (0.561 g/mL) at 4 °C. For specific, preferential fluorescence labeling of A-subunits, the precipitates were dissolved and dialyzed against 50 mM Bicine buffer with different gradients (pH 7.0–9.4) created by the addition of NaOH. Preferential labeling of B-subunits or the A-subunit of native holotoxin can be obtained under different pH profiles during the labeling (*SI Appendix*, Fig. S13*G*) (16).

DNA Constructs. The connexin isoforms used in this work, Cx30, Cx36, Cx43, and Cx45, were tagged at the C terminus with fluorescent proteins. Mouse Cx30 (NM_001010937), Cx36 (NM_010290), and Cx45 (NM_001159383.1) coding sequences were PCR-amplified from a mouse brain cDNA library using the following gene-specific primers (5′→3′): Cx30 forward: ATGGACTGGGGACCCTGC, Cx30 reverse: ACTTGGGAAACTTGTGATTGC; Cx36 forward: ATGGGGGAATGGACCATCTTG, Cx36 reverse: ACATAGGCAGAGTCACTGGAC; Cx45 forward: ATGAGTTGGAGCTTCCTGACTC, Cx45 reverse: AATCCAGACGGAGGTCTTCCC.

C-terminal in-frame ORF fusions were constructed using the pEGFP-N1, pEYFP-N1, or pECFP-N1 vectors (Clontech). C-terminally tagged Cx43 fluorescent proteins were described earlier (20). Actin-mRFP was a gift from Dr. Anna Akhmanova (Utrecht University, Utrecht, The Netherlands).

Measurement of cAMP Levels in Vero Cells Forming GJ Plaques During the Application of AB5 Toxins. Vero cells were transfected with a cAMP FRET-based sensor construct, CFP-Epac-YFP (26). Monolayer-grown Vero cells expressing the construct were washed with PBS, harvested, and homogenized in high-potassium/low-sodium Internal Medium (39, 41). Cell membranes were disrupted using G18, G22, and G27 injection needles, respectively. Fluorescence in drops of cellular homogenate (5 μL each) was imaged upon the addition of 1 μL of different concentrations (0.1 μM; 1 μM; 10 μM; 50 μM; 100 μM; 1 mM) of the cAMP analog 8-Bromo-cAMP, the mixed Epac/PKA agonist Sp-8-CPT-cAMPS, or the Epac agonist Sp-8-CPT-2′-O-MecAMPS (Sigma) but not PKA-specific agonist 6-Bnz-cAMP. Intensity images obtained with Optosplit

were used to calibrate cellular levels of cAMP under the same illumination/laser power and filter set based on Epac CFP/YFP FRET data.

Because cAMP is a short-lived molecule cleaved by cellular phosphodiesterases, in some experiments we used a cell-permeable, nonspecific inhibitor of cAMP and cGMP phosphodiesterases, IBMX. Forskolin (a cell-permeable diterpene from *Coleus forskohlii*) was used to raise the cellular level of adenylate cyclase in control experiments to image FRET dynamics and to recover possible increases in the cAMP level in Vero cells transfected with Epac sensor. Fluctuations of cAMP concentrations in Vero cells treated with forskolin (20 μM) and IBMX (500 μM) were measured over 10 h. First, to control for bleed-through between CFP and YFP channels, reference cells expressing only CFP or YFP were plated together with cells expressing the CFP-Epac-YFP construct. Then cells expressing only the CFP-Epac-YFP construct were plated together with cells expressing both the CFP-Epac-YFP construct and connexin-FP. These cells were imaged simultaneously in the same field of view using Optosplit (*SI Appendix*, Figs. S9 and S10), and fluorescence signals were compared. Three groups of images were collected: a donor image (CFP, excited at 440 nm and detected using a bandpass filter of 485/17 nm), a sensitized emission image (excited at 440 nm and detected using a bandpass filter of 525–560 nm), and the acceptor image (YFP, excited at 514 nm and detected using a bandpass filter of 525–560 nm). All images were corrected for donor leak-through into the sensitized emission channel (i.e., false acceptor excitation that may occur at 440 nm using correction factors derived from reference cell types). In some cases we decreased the excitation power of lasers or used narrow bandpass filters or a combination of both. To calculate FRET, we divided the sensitized emission image by the donor image using the MetaMorph 7.6 program with home-made macro routines.

Within 30–45 min after the addition of WT CTX, we observed a massive cAMP increase that was used as the maximal positive control for Vero cells. In some cells similar FRET levels also were obtained with forskolin, causing a significant decrease in FRET from E = 0.4–0.1. Interestingly, when two GJ-connected cells expressed CFP-Epac-YFP but only one of the two cells immobilized CTX, we observed similar FRET fluctuations in both cells. This effect likely is caused by the rapid diffusion of cAMP through GJs into the cytosol of the contacting cell.

Electrophysiology Recordings. Electrical coupling between cells expressing Cx36-EGFP was measured using a dual whole-cell voltage clamp (24, 42) before, during, and after the application of CTX. A pair of HeLa cells expressing Cx36-EGFP (cells 1 and 2) was voltage clamped at 0 mV. Junctional current (I_j) was measured in cell 1 in response to transjunctional voltage (V_j) applied to cell 2 in the form of repeated ramps changing from −30 to +30 mV over 1.3 s with the interval between ramps being 200 ms. Junctional conductance, g_j, was obtained from the ratio $g_j = -I_j/V_j$.

Inhibition of Synchronous cAMP Waves by the GJ Inhibitor Octanol. To confirm that synchronous waves of cAMP oscillations between coupled Cx30 cells indeed require GJ contacts (which are highly permeable to cAMP), we monitored cAMP signaling between coupled cells in control medium and in the presence of the GJ-uncoupling chemical octanol (10 mM). Cells transfected with both cAMP Epac FRET-sensor and Cx30-FP constructs were selected. In control coupled Cx30-FP cells, cAMP fluctuations maintained a similar maximum of intensity during the time intervals measured, whereas synchronous activity for cAMP disappeared in cells treated with octanol. Thus, GJ-coupled cells displayed similar coordinated oscillations because of the presence of GJ contacts. Synchronicity disappeared when GJ permeability was blocked. Similarly, electrical coupling disappeared quickly after the addition of decanol (Fig. 2*D*).

Treatment of Cells with Filipin and Latrunculin. Filipin (molecular formula: $C_{35}H_{58}O_{11}$; molecular weight, 654.83) purified from *Streptomyces filipinensis* was obtained from Sigma. Filipin was applied to cells expressing connexins labeled with fluorescent proteins at a concentration of 10 μg/mL for 20 min at 37 °C (43, 44). Binding of filipin to cholesterol (mostly dispersed in glycolipid microdomains) resulted in increased membrane fluorescence. We did not observe binding of AB5 toxins to GJ plaques, perhaps indicating that GB3 or GM1 that may be present in GJ plaques remained sterically protected from AB5 toxins, e.g., by the extracellular loops of connexins. Treatment with filipin generally increased the fluorescence of GJ plaques labeled with different FP-tagged connexin isoforms. Filipin thus is likely to enter the GJ plaques and possibly prevented the interaction of cholesterol with sphingolipids or lipid receptors. Treatment of Vero cells with 5–10 μg/mL filipin reduced or prevented the formation of tCDRs (mean ± SEM, data from four independent experiments, $^{**}P < 0.05$ vs. control, ANOVA). Latrunculin was used at a final concentration of 10 μM for 10 min at 37 °C to disassemble actin filaments (45).

Calibration of $[Ca^{2+}]$ Level in Living Vero Cells with Fluo-4 AM. To estimate cellular levels of $[Ca^{2+}]$, we used Fluo-4 AM (Invitrogen). Drops of a reference solution were recorded on the same coverslip and with the optical settings (laser power and bandpass of emission filters) later used for cell recordings. To calibrate the microscope setup, we used a reference solution prepared as a Ca^{2+} buffer [100 mM KCl, 30 mM 3-(*N*-morpholino)propanesulfonic acid (Mops), 10 mM K^2.EGTA, and 2 mM Ca^{2+}-EGTA (pH 7.2)], which is expected to have a free $[Ca^{2+}]$ level below 50 nM. To this solution 5 μM Fluo-4 AM (final concentration) was added, and a drop (2–5 μL) of this solution was recorded under settings [i.e., laser excitation/emission (λ ex/em), filter set, and coverslips] identical to those used for imaging cells.

To measure toxin-induced intracellular Ca^{2+}, Vero cells were preloaded with Fluo-4 AM. Culture medium was removed from cells grown on coverslips in six-well plates and was replaced by DMEM with 100 μL of 4 μM Fluo-4 AM per coverslip, and cells were incubated for 1 h at 37 °C. After nonfluorescent ester was incorporated into Vero cells, the incubation medium was removed, and coverslips were transferred into experimental chambers with fresh medium. Images were taken with an Andor CCD camera (4 s) using a narrow bandpass (510/10 nm) while cells were treated with Cy5-labeled fluorescent toxins (100 ng/mL) as indicated. Finally extracellular calcium (5 mM), or ATP (5 mM) was used as a control to reveal the highest amount of intracellular calcium. To estimate concentrations of intracellular calcium in Vero cells, we used the calculation $[Ca^{2+}] = K_d \times (Iexp - Imin)/(Imax - Iexp)$, where K_d is the affinity of the Fluo-4 AM for calcium [according to the manufacturer (Life Technologies), $K_d = 0.345$ $pmol^{-1}$], Iexp is the fluorescence measured using a bandpass of 510/10 nm, Imin is the cell fluorescence in the absence of calcium, and Imax is the fluorescence when calcium was saturated with 5 mM of extracellular calcium. To determine I_{max}, cells were lysed on the coverslip with 2% of Triton-X100 to demonstrate calcium saturation. Finally, 10 mM EGTA was used to quench the signal to base level.

Because the intracellular esterases may cleave Fluo-4 AM into Fluo-4, we controlled the level of intracellular calcium by incubating a control set of cells with a solution containing the calcium ionophore A23187 and known concentrations of $[Ca^{2+}]$. We were aware that Fluo4 potentially binds Ca^{2+} extensively during the application of AB5 toxins and can act as a local buffer that could secondarily alter the local Ca^{2+} concentration to modulate the original Fluo-4 AM–based Ca^{2+}-dependent fluorescence signal (*SI Appendix*, Fig. S7).

Image Analysis. Fluorescence images were analyzed using MetaMorph 7.6 (www.moleculardevices.com/) as described (21, 37). For the line scan or region of interest fluorescence measurements, the average value projections were created from individual *z*-stacks in Tiff or AVI format, and the background was subtracted for each image. To calculate the number of tCDRs formed during experiments, we used the Maple 14 program (Maplesoft).

Statistical Analyses. Data presented were replicated in five or more independent experiments. Statistical analyses were performed using a two-tailed Student *t* test assuming equal variances. Multiple group comparison at the same time was done using single-factor ANOVA. Generally, $P < 0.05$ was considered significant, and the obtained *P* values were estimated if statistically significant differences were required. The estimated amount and diameter of the tCDR profiles was approximated on the basis of magnification scales used. The scaling ratio was obtained from linear fits to the data.

ACKNOWLEDGMENTS. We thank Dr. Christian Hübner for help with fluorescence spectroscopy measurements; Dr. Klaus Aktories for providing CNF toxin; Dr. Anna Akhmanova for the actin- and EB3-mCherry constructs; Dr. Manuela Zaccolo for cytosolic and membrane-attached Epac-based cAMP sensors; Drs. James Pawley, Michael Berridge, Richard Blumberg, Werner W. Franke, and Rolf Hilgenfeld for discussions; and Robert Schönherr and Dr. Enno Hartmann for comments on versions of the manuscript. This study was supported by a Deutsche Forschungsgemeinschaft Excellence Cluster ''Inflammation at Interfaces'' grant (to R.D.) and by National Institutes of Health Grants NS55363 (to M.V.L.B.) and NS72238 and HL84464 (to F.B.). M.V.L.B. is the Sylvia and Robert S. Olnick Professor of Neuroscience and Distinguished Professor of the Albert Einstein College of Medicine.

1. Gilula NB, Reeves OR, Steinbach A (1972) Metabolic coupling, ionic coupling and cell contacts. *Nature* 235(5336):262–265.

2. Goodenough DA, Goliger JA, Paul DL (1996) Connexins, connexons, and intercellular communication. *Annu Rev Biochem* 65:475–502.

3. Yeager M, Nicholson BJ (1996) Structure of gap junction intercellular channels. *Curr Opin Struct Biol* 6(2):183–192.
4. Bennett MV, Zukin RS (2004) Electrical coupling and neuronal synchronization in the Mammalian brain. *Neuron* 41(4):495–511.
5. Connors BW, Long MA (2004) Electrical synapses in the mammalian brain. *Annu Rev Neurosci* 27:393–418.
6. Goldberg GS, Lampe PD, Nicholson BJ (1999) Selective transfer of endogenous metabolites through gap junctions composed of different connexins. *Nat Cell Biol* 1(7): 457–459.
7. Goldberg GS, Valiunas V, Brink PR (2004) Selective permeability of gap junction channels. *Biochim Biophys Acta* 1662(1-2):96–101.
8. Yeager M, Harris AL (2007) Gap junction channel structure in the early 21st century: Facts and fantasies. *Curr Opin Cell Biol* 19(5):521–528.
9. Harris AL (2007) Connexin channel permeability to cytoplasmic molecules. *Prog Biophys Mol Biol* 94(1-2):120–143.
10. Alev C, et al. (2008) The neuronal connexin36 interacts with and is phosphorylated by CaMKII in a way similar to CaMKII interaction with glutamate receptors. *Proc Natl Acad Sci USA* 105(52):20964–20969.
11. Segretain D, Falk MM (2004) Regulation of connexin biosynthesis, assembly, gap junction formation, and removal. *Biochim Biophys Acta* 1662(1-2):3–21.
12. Gaietta G, et al. (2002) Multicolor and electron microscopic imaging of connexin trafficking. *Science* 296(5567):503–507.
13. Jordan K, Chodock R, Hand AR, Laird DW (2001) The origin of annular junctions: A mechanism of gap junction internalization. *J Cell Sci* 114(Pt 4):763–773.
14. Nickel B, et al. (2013) Visualizing the effect of dynamin inhibition on annular gap vesicle formation and fission. *J Cell Sci* 126(Pt 12):2607–2616.
15. Planchon TA, et al. (2011) Rapid three-dimensional isotropic imaging of living cells using Bessel beam plane illumination. *Nat Methods* 8(5):417–423.
16. Majoul IV, Bastiaens PI, Söling HD (1996) Transport of an external Lys-Asp-Glu-Leu (KDEL) protein from the plasma membrane to the endoplasmic reticulum: Studies with cholera toxin in Vero cells. *J Cell Biol* 133(4):777–789.
17. Majoul I, et al. (1998) KDEL receptor (Erd2p)-mediated retrograde transport of the cholera toxin A subunit from the Golgi involves COPI, p23, and the COOH terminus of Erd2p. *J Cell Biol* 143(3):601–612.
18. Majoul I, et al. (2002) Differential expression of receptors for Shiga and Cholera toxin is regulated by the cell cycle. *J Cell Sci* 115(Pt 4):817–826.
19. Windschiegl B, et al. (2009) Lipid reorganization induced by Shiga toxin clustering on planar membranes. *PLoS ONE* 4(7):e6238.
20. Butkevich E, et al. (2004) Drebrin is a novel connexin-43 binding partner that links gap junctions to the submembrane cytoskeleton. *Curr Biol* 14(8):650–658.
21. Majoul IV, et al. (2009) Limiting transport steps and novel interactions of Connexin-43 along the secretory pathway. *Histochem Cell Biol* 132(3):263–280.
22. Falk MM, Baker SM, Gumpert AM, Segretain D, Buckheit RW, 3rd (2009) Gap junction turnover is achieved by the internalization of small endocytic double-membrane vesicles. *Mol Biol Cell* 20(14):3342–3352.
23. Lingwood D, Simons K (2010) Lipid rafts as a membrane-organizing principle. *Science* 327(5961):46–50.
24. Bukauskas FF, Bukauskiene A, Bennett MV, Verselis VK (2001) Gating properties of gap junction channels assembled from connexin43 and connexin43 fused with green fluorescent protein. *Biophys J* 81(1):137–152.
25. Lo WK, Mills A, Kuck JF (1994) Actin filament bundles are associated with fiber gap junctions in the primate lens. *Exp Eye Res* 58(2):189–196.
26. Ponsioen B, et al. (2004) Detecting cAMP-induced Epac activation by fluorescence resonance energy transfer: Epac as a novel cAMP indicator. *EMBO Rep* 5(12): 1176–1180.
27. Piehl M, et al. (2007) Internalization of large double-membrane intercellular vesicles by a clathrin-dependent endocytic process. *Mol Biol Cell* 18(2):337–347.
28. Bang B, Gniadecki R, Gajkowska B (2005) Disruption of lipid rafts causes apoptotic cell death in HaCaT keratinocytes. *Exp Dermatol* 14(4):266–272.
29. George KS, Wu S (2012) Lipid raft: A floating island of death or survival. *Toxicol Appl Pharmacol* 259(3):311–319.
30. Biswas SK, Jiang JX, Lo WK (2009) Gap junction remodeling associated with cholesterol redistribution during fiber cell maturation in the adult chicken lens. *Mol Vis* 15:1492–1508.
31. Mukherjee S, Zha X, Tabas I, Maxfield FR (1998) Cholesterol distribution in living cells: Fluorescence imaging using dehydroergosterol as a fluorescent cholesterol analog. *Biophys J* 75(4):1915–1925.
32. McGookey DJ, Fagerberg K, Anderson RG (1983) Filipin-cholesterol complexes form in uncoated vesicle membrane derived from coated vesicles during receptor-mediated endocytosis of low density lipoprotein. *J Cell Biol* 96(5):1273–1278.
33. Damm EM, et al. (2005) Clathrin- and caveolin-1-independent endocytosis: Entry of simian virus 40 into cells devoid of caveolae. *J Cell Biol* 168(3):477–488.
34. Kinsky SC (1970) Antibiotic interaction with model membranes. *Annu Rev Pharmacol* 10:119–142.
35. Hendrix DL, Higinbotham N (1973) Effects of filipin and cholesterol on K movement in etiolated stem cells of Pisum sativum L. *Plant Physiol* 52(2):93–97.
36. Maurer UE, Sodeik B, Grünewald K (2008) Native 3D intermediates of membrane fusion in herpes simplex virus 1 entry. *Proc Natl Acad Sci USA* 105(30):10559–10564.
37. Majoul I, Straub M, Hell SW, Duden R, Söling HD (2001) KDEL-cargo regulates interactions between proteins involved in COPI vesicle traffic: Measurements in living cells using FRET. *Dev Cell* 1(1):139–153.
38. Kozlov YV, Chernaia MM, Fraser ME, James MN (1993) Purification and crystallization of Shiga toxin from Shigella dysenteriae. *J Mol Biol* 232(2):704–706.
39. Melton-Celsa A, Mohawk K, Teel L, O'Brien A (2012) Pathogenesis of Shiga-toxin producing escherichia coli. *Curr Top Microbiol Immunol* 357:67–103.
40. van den Akker F, Pizza M, Rappuoli R, Hol WG (1997) Crystal structure of a non-toxic mutant of heat-labile enterotoxin, which is a potent mucosal adjuvant. *Protein Sci* 6(12):2650–2654.
41. Majoul I, Jia Y, Duden R (2006) *Handbook of Biological Confocal Microscopy*, ed Pawley JB (Springer, New York), 3rd Ed, pp 788–808.
42. Skeberdis VA, Rimkute L, Skeberdyte A, Paulauskas N, Bukauskas FF (2011) pH-dependent modulation of connexin-based gap junctional uncouplers. *J Physiol* 589(Pt 14): 3495–3506.
43. Bergy ME, Eble TE (1968) The filipin complex. *Biochemistry* 7(2):653–659.
44. Orlandi PA, Fishman PH (1998) Filipin-dependent inhibition of cholera toxin: Evidence for toxin internalization and activation through caveolae-like domains. *J Cell Biol* 141(4):905–915.
45. Coué M, Brenner SL, Spector I, Korn ED (1987) Inhibition of actin polymerization by latrunculin A. *FEBS Lett* 213(2):316–318.